optical depth and the range of permissible particle sizes.
15. W. M. Irvine, *J. Geophys. Res.* **71**, 2931 (1966).
16. Theoretical studies, laboratory experiments, and astronomical observations of other objects in the solar system have shown that a determination of the phase curve is important in understanding the physical nature (composition, particle size, and degree of compaction) of a planetary regolith [B. W. Hapke, *Astron. J.* **71**, 333 (1966); J. Veverka, in *Planetary Satellites*, J. Burns, Ed. (Univ. of Arizona Press, Tucson, 1977), pp. 171–209]. Especially important is the opposition surge at small phase angles (<6°). Previous ground-based observations of the Uranian satellites have been limited, of necessity, to solar phase angles of less than 3°0 [R. H. Brown and D. P. Cruikshank, *Icarus* **55**, 83 (1983)], and therefore the full solar phase angle range of the opposition surge region was unknown before this study. The conventional explanation of the opposition surge is that mutual shadowing among the particles in the optically active portion of the regolith disappears as the face of the object becomes illuminated to the observer. In general, fluffy surfaces exhibit greater opposition surges.
17. B. J. Buratti and J. Veverka, *Icarus* **58**, 254 (1984); B. J. Buratti, *ibid.* **59**, 392 (1984).
18. R. M. Nelson *et al.*, in preparation.
19. R. M. Nelson and B. W. Hapke, *Icarus* **36**, 304 (1978).
20. M. Noland *et al.*, *ibid.* **23**, 334 (1974).
21. We thank the members of the Voyager flight team, who made possible the successful encounter of the PPS with Uranus; P. D. Nicholson and J. Colwell for timing of the predicted occultation events; and M. D. Morrison (JPL) and A. Bahrami (LASP) for exceptional software wizardry. We also thank NASA's Office of Information Systems (code EI) Pilot Planetary Data System Project at the Jet Propulsion Laboratory for computational assistance in the rapid transformation of flight telemetry into scientific results.

31 March 1986; accepted 5 May 1986

Infrared Observations of the Uranian System

R. HANEL, B. CONRATH, F. M. FLASAR, V. KUNDE, W. MAGUIRE, J. PEARL, J. PIRRAGLIA, R. SAMUELSON, D. CRUIKSHANK, D. GAUTIER, P. GIERASCH, L. HORN, P. SCHULTE

The infrared interferometer spectrometer (IRIS) on Voyager 2 recorded thermal emission spectra of Uranus between 200 and 400 cm^{-1} and of Miranda and Ariel between 200 and 500 cm^{-1} with a spectral resolution of 4.3 cm^{-1}. Reflected solar radiation was also measured with a single-channel radiometer sensitive in the visible and near infrared. By combining IRIS spectra with radio science results, a mole fraction for atmospheric helium of 0.15 ± 0.05 (mass fraction, 0.26 ± 0.08) is found. Vertical temperature profiles between 60 and 900 millibars were derived from average polar and equatorial spectra. Temperatures averaged over a layer between 400 to 900 millibars show nearly identical values at the poles and near the equator but are 1 or 2 degrees lower at mid-latitudes in both hemispheres. The cooler zone in the southern hemisphere appears darker in reflected sunlight than the adjacent areas. An upper limit for the effective temperature of Uranus is 59.4 kelvins. Temperatures of Miranda and Ariel at the subsolar point are 86 ± 1 and 84 ± 1 kelvins, respectively, implying Bond albedos of 0.24 ± 0.06 and 0.31 ± 0.06, respectively. Estimates of phase integrals suggest that these satellites have unusual surface microstructure.

DURING THE VOYAGER 2 ENCOUNTER, Uranus, Miranda, and Ariel were investigated by Voyager's infrared interferometer spectrometer (IRIS), which recorded thermal emission spectra between approximately 200 and 400 cm^{-1} (25 and 50 μm) and reflected solar radiation in the visible and near infrared. IRIS consists of a Michelson interferometer, which covers the thermal spectrum with a resolution of 4.3 cm^{-1}, and a bore-sighted, single-channel radiometer sensitive between 0.4 and 1.5 μm (*1*). Both devices share a 50-cm Cassegrain telescope with a common circular field of view of 0.125° half-cone angle. Absolute calibration of the interferometer is accomplished by scaling the planetary and satellite spectra at each wavenumber interval to deep space spectra and maintaining the instrument at 200 ± 0.1 K. The radiometer is calibrated by occasionally viewing a diffuse reflector exposed to sunlight. IRIS results for the Jovian and Saturnian systems have been summarized (*2*). We now present initial results for Uranus and two of its satellites; we obtained no useful information about the rings.

The brightness spectrum of Uranus. The signal-to-noise ratio (S:N) for an individual Voyager 2 spectrum is greater than 1 between 190 and 320 cm^{-1} and reaches a maximum of about 8 at approximately 230 cm^{-1}. For most purposes we wished to increase this ratio by averaging spectra; the improvement in S:N is proportional to the square root of the number of spectra included in the average. Thus for the averages of south polar and equatorial spectra (Fig. 1), the maximum value of S:N is 195 and 90, respectively.

The thermal spectrum of Uranus is determined by the He abundance, the para-hydrogen fraction, the vertical atmospheric temperature profile, and the properties and vertical distribution of clouds. In principle, all these parameters may be extracted from sufficiently precise spectral measurements, although the solutions are not necessarily unique.

Helium abundance. The atmospheric He abundance can be obtained from the shape of the thermal spectrum or from a comparison of IRIS spectra with RSS data. For both methods, the equatorial spectrum of Fig. 1 (recorded at 5°S, the approximate latitude of the radio occultation points) was used. First, we examined the sensitivity of the spectral shape to various atmospheric parameters. A reference spectrum was calculated for an emission angle of 57°, for a He mole fraction of 0.15, for an equilibrium para-hydrogen fraction, and without the effects of CH_4 gas or clouds. Each parameter was then varied to test the effect on the spectrum. Collision-induced absorption coefficients for H_2–H_2, H_2–He, and H_2–CH_4 were calculated as described (*3*) with the incorporation of recent improvements from laboratory data.

The effect of He abundance variations is shown in Fig. 2. In an atmosphere composed of H_2 and He, an opacity minimum occurs near 200 cm^{-1} as a result of the relative strength of the pressure-induced $S(0)$ transition of H_2 and the translational H_2 opacity, which is strongly affected by collisions of H_2 molecules with He atoms. The position of the resulting brightness temperature maximum depends only weakly on atmospheric temperature but strongly on the He abundance. The broad maximum shifts to higher wavenumbers with increasing He concentration. The position of the maximum also depends strongly on the para-hydrogen fraction (Fig. 3). This fraction is expected to lie between the high-temperature limit or normal value (0.25) and the equilibrium value for the ambient atmospheric temperature. The maximum shifts to higher wavenumbers with decreasing para-hydrogen fraction.

The effect of gaseous CH_4 at the maxi-

R. Hanel, B. Conrath, F. M. Flasar, V. Kunde, W. Maguire, J. Pearl, J. Pirraglia, R. Samuelson, Laboratory for Extraterrestrial Physics, NASA Goddard Space Flight Center, Greenbelt, MD 20771.
D. Cruikshank, Institute of Astronomy, University of Hawaii, Honolulu, HI 96822.
D. Gautier, Paris Observatory, 92190 Meudon, France.
P. Gierasch, Department of Astronomy, Cornell University, Ithaca, NY 14853.
L. Horn and P. Schulte, Jet Propulsion Laboratory, California Institute of Technology, Pasadena, CA 91109.

mum amount permissible by the vapor pressure law is to lower the brightness temperature by less than 0.7 K between 175 and about 230 cm^{-1} and by negligible amounts above 250 cm^{-1}. No significant shift of the maximum occurs. Methane clouds can also affect the spectral shape. Figure 4 shows the results from anisotropic multiple-scattering calculations for two mean particle radii (r), 3 and 30 μm. The cloud bases are set at 1.3 bar and the scale heights at 10 km. Number densities were adjusted to force a 2 K brightness temperature difference at 200 cm^{-1} between the cloud models and the standard cloud-free reference spectrum. It was verified that the abundance of condensate nowhere exceeded the assumed vapor-phase mole fraction of 0.025 at the cloud base. Between 175 and 300 cm^{-1} the spectral shape is affected strongly by particle size but only weakly by cloud scale height.

Of the four mechanisms affecting the shape of the spectrum, CH_4 vapor and clouds probably play the least important roles. A good fit to the observed spectrum at the radio occultation point can be found from the radio occultation profile on the assumption of cloud-free conditions. A substantial additional opacity due to CH_4 clouds is difficult to accommodate. There is no compelling evidence of any influence of CH_4 clouds on the observed spectra, which leaves only the He abundance and the para-hydrogen fraction as significant known factors.

The dependence of the spectral position of the temperature maximum on the He abundance and the para-hydrogen fraction is shown in Fig. 5. Since the atmospheric para-hydrogen fraction is not expected to exceed the equilibrium value, the wavenumber of the maximum brightness temperature places an upper limit on the He mole fraction. The shape of the spectrum near 200 cm^{-1} and the low value of S:N below that wavenumber (Fig. 1) prevent a precise determination of the maximum. However, values above 215 cm^{-1} appear to be excluded, suggesting that the solution lies within the shaded area of Fig. 5. Consequently the para-hydrogen fraction must be close to equilibrium (certainly larger than 0.5), and the He mole fraction cannot exceed about 0.15. Uncertainties in the absorption coefficients used in the model, and errors due to the preliminary calibration, can modify the shape of the spectrum in this region. A mole fraction of 0.4, as recently suggested (*4*), can be ruled out, however.

A more sensitive determination of the He abundance was achieved by combining the IRIS spectral measurements with the radio occultation results, as was done for Jupiter and Saturn (*5, 6*). The RSS measurements yield the ratio of temperature to mean molecular weight (T:M) as a function of pressure, provided that the composition is uniform with altitude. This profile can be used to calculate theoretical spectra for various values of the mean molecular weight; the true atmospheric He fraction is then determined from the best fit to the measured spectrum. In most levels of the atmosphere to which the spectral measurements are sensitive, only H_2 and He contribute significantly to the mean molecular weight, so that the He abundance can be inferred directly. The CH_4 abundance is limited by the saturation law and can only contribute significantly to the mean molecular weight at pressures greater than about 700 mbar; gases heavier than He would lower the derived He abundance.

Figure 6 shows theoretical spectra for

Fig. 1 (top). Measured brightness temperature spectra (solid curves) of the south polar area (average of 597 individual spectra) and at 5°S latitude (equator, average of 125 individual spectra). The emission angles are 15° and 57°, respectively; this difference in emission angle accounts almost entirely for the difference between the curves. Below 200 cm^{-1} and above 300 cm^{-1}, random noise is strongly evident. Theoretical spectra (broken curves) calculated from retrieved temperature profiles are shown for comparison. Fig. 2 (bottom). Calculated spectra for different mole fractions of He. The radio occultation profile and an equilibrium para-hydrogen fraction are assumed; effects of CH_4 gas and clouds are neglected.

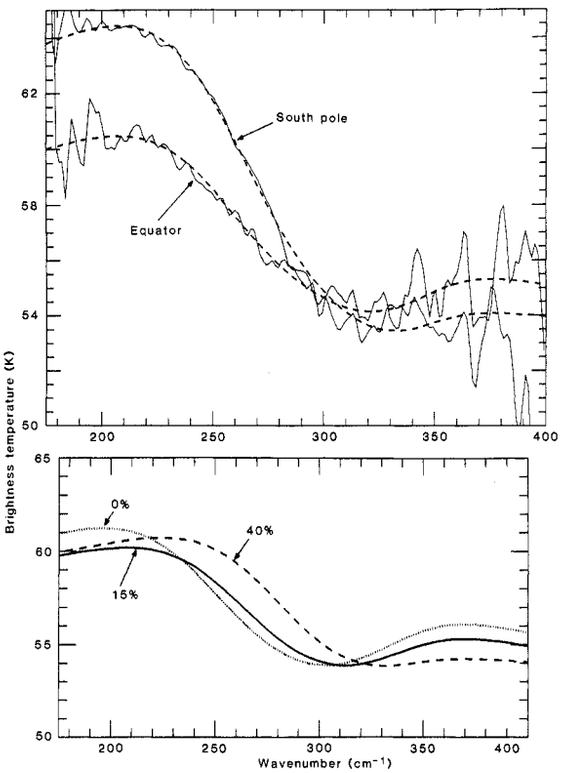

Fig. 3 (top). Calculated spectra for different para-hydrogen fractions. The normal value (0.25) is expected to exist in the planetary interior, where temperatures are greater than 300 K. The equilibrium value (0.62) is for the ambient temperature and is applicable to the levels probed. An intermediate value (0.45) is also shown. An He mole fraction of 0.15 and clear atmospheric conditions are assumed. Fig. 4 (bottom). Calculated spectra showing the variations in CH_4 clouds with particle size distributions, which peak at 3 and 30 μm. A cloud base at 1.3 bars and a cloud scale height of 10 km were assumed. The number density at the cloud base has been adjusted to provide a brightness temperature 2 K lower than the standard cloud-free model at 200 cm^{-1}.

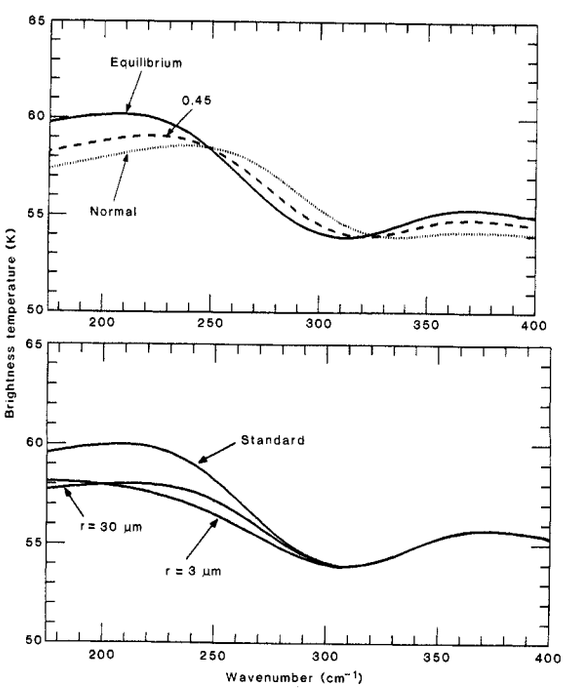

three values of the He mole fraction that were calculated from an initial *T:M* profile provided by the Voyager RSS team (*7*). Also shown is the equatorial spectrum from Fig. 1, which was obtained at nearly the same latitude as the RSS data. The principal sensitivity of the theoretical spectra to the He abundance is through the molecular weight, with a small additional effect due to the H_2–He contribution to the atmospheric opacity. An equilibrium para-hydrogen fraction was assumed, and a gaseous CH_4 distribution in accordance with the saturation law was introduced. The latter was included because of the small H_2–CH_4 contribution to the collision-induced opacity in the spectral region near 200 cm^{-1} and the contribution of CH_4 to the mean molecular weight at deeper levels. The best overall fit to the spectrum is achieved with a He mole fraction of about 0.155. This value, combined with the constraint imposed by the location of the brightness temperature maximum, justifies the assumption of an equilibrium para-hydrogen fraction.

Several possible sources of error exist in the determination that can be only partially evaluated: uncertainty in the initial radio occultation profile, errors in the IRIS measurements, uncertainties in the H_2–He absorption coefficients, and lack of temperature information at pressures lower than 10 mbar. As judged from estimates of these factors, the He mole fraction is 0.15 ± 0.05 (He mass fraction, 0.26 ± 0.08). Thus, the He mass fraction determined for Uranus is larger than that for Jupiter (0.18 ± 0.04) and Saturn (0.06 ± 0.05) (*6*). Although the proto-solar He abundance is uncertain (*6*), most recent estimates from solar evolutionary models (*8*) as well as from measurements of solar oscillations (*9*) suggest a mass fraction of about 0.28, in agreement with the value for Uranus. If this is the He mass fraction for the primordial solar nebula, then not only has differentiation of He from metallic hydrogen occurred in Saturn, but it has also begun in Jupiter.

Atmospheric temperature and dynamics. Averaging of various sets of spectra from the polar and equatorial regions yield sufficiently high S:N to permit retrieval of temperature profiles (Fig. 7). In Fig. 1, two of the averaged spectra are compared with calculations based on the retrieved profiles. A He mole fraction of 0.15 and an equilibrium para-hydrogen fraction were assumed; possible opacity effects due to clouds and gaseous CH_4 were neglected. The polar spectra provide information about the thermal structure at pressures between about 60 and 900 mbar; the equatorial spectra were taken at high emission angle and do not probe pressures greater than 600 mbar. At pressures less than 60 mbar, the retrievals had to blend smoothly into an estimated profile that is based on a recent analysis of ground-based data (*10*).

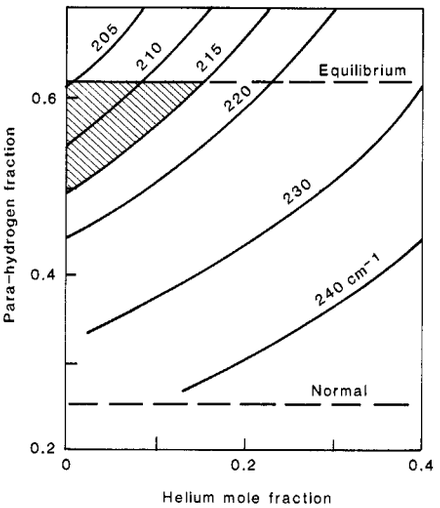

Fig. 5. Calculated position of the brightness temperature maximum as a function of He mole fraction and para-hydrogen fraction. The hatched area represents the constraint imposed by the measured spectra. The indicated equilibrium value of the para-hydrogen fraction is for a temperature of 64 K; the normal value is the high temperature limit. Methane gas and aerosol opacities were omitted.

The general character of the profiles is consistent with Earth-based results (*10, 11*). The derived profiles are remarkably similar to each other. In the lower stratosphere the dark pole is 2 to 3 K warmer than the illuminated pole, but this must be regarded with caution because possible errors in the currently available pointing geometry and uncertainties in the initial radiometric calibration of the data acquired from the dark hemisphere can affect the results.

At pressures greater than approximately 600 mbar, the retrieved polar profiles are consistent with lapse rates that exceed the adiabatic value for the equilibrium para-hydrogen fraction; the inclusion of additional opacity due to gaseous CH_4 or clouds would further increase the inferred temperature gradients. The radio occultation results also imply a lapse rate in this part of the atmosphere in excess of the equilibrium adiabat, approaching the frozen equilibrium value in which the ortho and para modifications of H_2 behave as a thermally noninteracting gas mixture. These results cannot presently be reconciled with the inferred near-equilibrium para-hydrogen fraction.

The weak thermal emission from Uranus prevents retrieval of complete temperature profiles from individual spectra, as was done for Jupiter and Saturn. Instead, limited temperature information was extracted by fitting a second-degree polynomial to the 200- to 275-cm^{-1} region and then taking the brightness temperature at 225 cm^{-1}. For normal viewing, this brightness temperature represents the mean atmospheric temperature between approximately 400 and 900 mbar. Data acquired at other emission angles were adjusted to normal viewing; for the location of each measurement a theoretical 225-cm^{-1} brightness temperature was computed from the temperature profile retrieved from the south polar region (Fig. 7). The difference between theoretical and measured temperatures was then subtracted from the calculated brightness temperature for normal viewing to yield an estimate of the atmospheric temperature in the 400- to 900-mbar region. The approach assumes that the relative shape of the profile in this part of the atmosphere is independent of location.

This method was applied to data acquired from two meridional scans that provide pole-to-pole coverage. The results (Fig. 8b) indicate an asymmetry between hemispheres with a temperature minimum near 25°S and a weaker minimum at approximately 40°N. As noted above, radiative transfer calculations indicate that a 2 K decrease in bright-

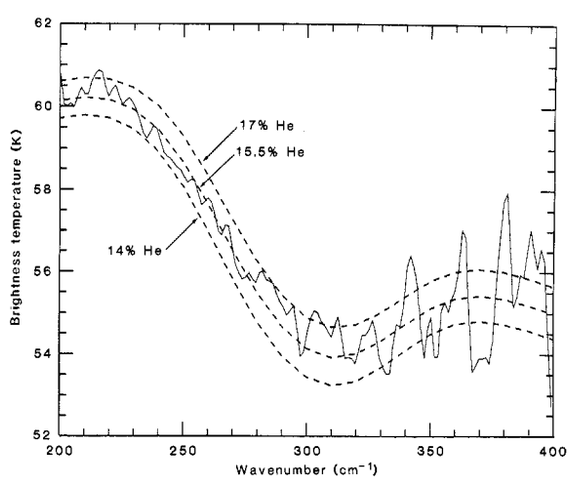

Fig. 6. Comparison of theoretical spectra (broken curves) and an average of 125 measured spectra (solid curve) taken near 5°S latitude (also shown in Fig. 1). The theoretical spectra were calculated from an initial radio occultation profile scaled for the values of the He mole fraction shown.

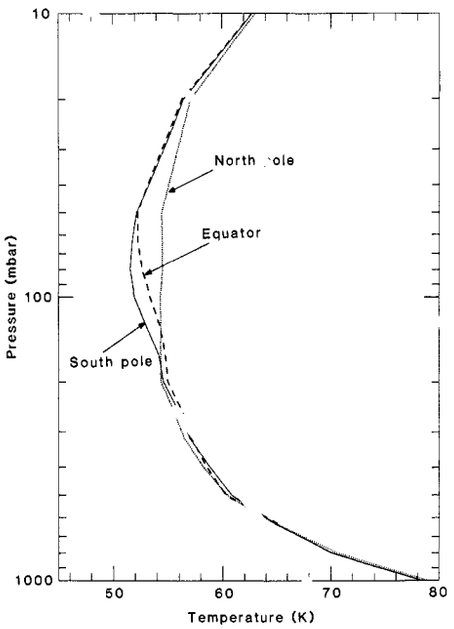

Fig. 7. Temperatures retrieved from averaged spectra at three locations on Uranus: the south (illuminated) pole (597 spectra), the north (dark) pole (100 spectra), and 5°S latitude, which is close to the latitudes of the radio occultation soundings (125 spectra).

ness temperature relative to a clear atmosphere can be obtained with reasonable cloud models and constant kinetic temperatures. To determine whether the apparent temperature variations represent actual kinetic temperature gradients or variations in cloud opacity, we used radiometer data taken simultaneously with the thermal spectra. Because the radiometer data encompass a range in both solar and emission angle, it was necessary to reduce the measurements to equivalent values for a standard observational geometry. The radiometer data are well fitted by a Minnaert law of the form $I = I_0 \mu_0^{k} \mu^{k-1}$ with $k = 0.84$. This expression was used with individual radiance measurements I to calculate I_0, the equivalent radiance for $\mu = \mu_0 = 1$, where μ and μ_0 are the cosines of the emission and solar zenith angles, respectively. Results from the latitude scan are shown in Fig. 8a. The correlation of the minimum in the radiometer data with the temperature minimum near 25° latitude suggests that the cooler temperatures are not the result of a cloud opacity effect, since regions of relatively dense cloud should appear relatively bright in reflected light.

The inferred latitudinal temperature structure probably results from a combination of radiative and dynamic effects. If purely radiative, the equilibrium temperature at 400 to 900 mbar would be about 7 K warmer at both poles than at the equator (*12*). Since the radiative time constant is long (approximately 200 years), the temperature responds primarily to the annual mean insolation, which is a maximum at the poles because of the 82° obliquity of the planet. The measured temperature structure deviates markedly from such behavior, and the small overall contrast of about 2 K suggests a dynamical redistribution of heat. Moreover, the minimum temperatures occur not at the equator but at mid-latitudes.

In a rapidly rotating atmosphere, the thermal wind equation relates the vertical gradient of the zonal wind speed to the latitudinal gradient of the temperature along a constant pressure surface (*13*). Applying this relation to the smoothed temperatures in Fig. 8b yields the vertical wind shear shown in Fig. 8c. A positive shear means that a positive zonal wind (in the direction of the planetary rotation) will increase with height. Positive winds have been deduced from tracking cloud images at latitudes of 27°, 35°, 40°, and 71° (*14*). The points between 27° and 40° are in a region of negative vertical shear, where the winds must be decaying with height between 400 and 900 mbar; at 71° the shear is essentially zero. An anticorrelation between thermal wind shear and winds derived from cloud motion was found on both Jupiter and Saturn, indicating a decay of the zonal jets with height in the upper troposphere. If such a relation is assumed to hold everywhere on Uranus, then the thermal wind shears of Fig. 8c imply the existence of a hemispherically asymmetric system of large-scale jets with strong negative winds at low latitudes. In contrast, the equatorial jets on both Jupiter and Saturn are in the direction of planetary rotation. The reversed sense of the winds on Uranus might be associated with the reversed gradient in the mean insolation.

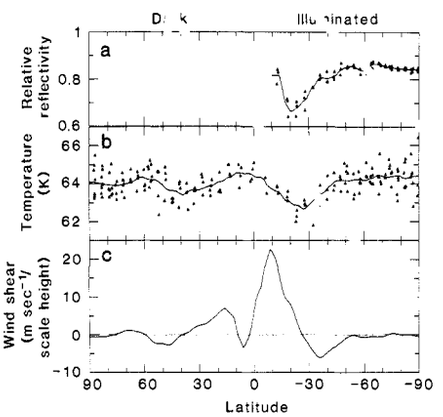

Fig. 8. Pole-to-pole latitude scans compiled from two sequences of observations. (a) Relative reflectivity normalized to vertical viewing by fitting a Minnaert law ($k = 0.84$). (b) Brightness temperature at 225 cm^{-1}, normalized to vertical viewing. In (a) and (b) the triangles denote the individual data, and the solid curves are running means with latitude bins 5° wide (a) and 15° wide (b). (c) Zonal thermal wind shear computed from the solid curve in (b) and then subjected to an additional running mean of 15° bin width.

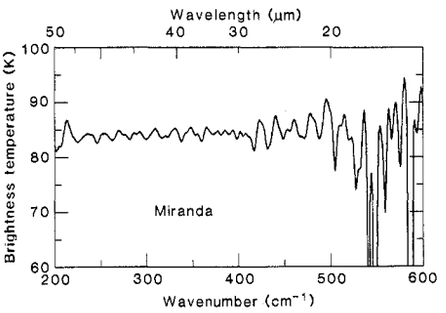

Fig. 9. Brightness temperature spectrum of Miranda near the south pole. The fine structure in the spectrum is noise. In this average of three individual spectra, S:N drops to 1 just beyond 500 cm^{-1}.

The latitudes of lower temperatures could logically be associated with upward motion and adiabatic cooling, which is consistent with the decay of jets with height as the result of a momentum-damping mechanism (*15*). However, if the radiometer responds to clouds formed by condensation of CH_4, then enhanced radiometer readings would be expected in the cooler upwelling regions. The opposite is actually observed. In this sense Uranus is more like Saturn—where regions of high albedo do not correlate well with low temperatures—than like Jupiter—where regions of high albedo and low temperature usually coincide. Alternatively, the radiometer may respond to a high-altitude haze, not directly associated with CH_4 condensation, that is reduced in thickness at latitudes equatorward of 40°.

Effective temperature. The determination of the planetary effective temperature requires integration of the thermal disk emission over all directions and all wavenumbers. As a first approximation, the temperature profile derived from the south polar spectrum, Fig. 1, was used to calculate the effective temperature. This is possible because Uranus seems to be uniform in its temperature in the region of the atmosphere (~400 mbar) from which most of the radiant energy emerges. An upper limit of 59.4 K for the effective temperature was obtained.

Satellites. Only Miranda and Ariel were spatially resolved by IRIS; during the observations reported here their apparent diameters were approximately three times the projected diameter of the instrument's field of view; the phase angles were 36° for Miranda and 31° for Ariel. Observed near the subsolar point (the south polar region), the thermal spectra show useful signal to about 500 cm^{-1}; no spectral features are evident above the noise (Fig. 9). The maximum brightness temperatures, T_{ss}, were 86 ± 1 K and 84 ±

1 K for Miranda and Ariel, respectively. From the relation $A = 1 - R^2(T_{ss}/T_0)^4$ (where A is the local albedo), the bolometric albedos in the south polar regions of the two objects are therefore 0.23 ± 0.06 and 0.30 ± 0.05, respectively. Here, R is the distance from Uranus to the sun [19.122 astronomical units (AU)], and the radiative properties of the satellites are assumed to be uniform. T_0, the subsolar point equilibrium temperature for 0° phase angle at 1 AU, would be 395 K for a Lambertian surface. However, peaking of the infrared emission at low phase angles leads to an observed value of 400 K for Earth's moon (*16*), while observations of other satellites and of asteroids suggest values as high as 408 K. For the present calculations, we adopt 401 ± 6 K for T_0.

To determine the Bond albedos (A_B) from the local albedos (A) requires knowledge of the surface phase function. On the basis of a surface-scattering model, Goguen (*17*) estimates that for two extreme cases of surface microstructure—strongly backscattering, low-albedo grains and isotropically scattering, high-albedo grains—A_B/A varies from 1.0 to 1.1. Adopting the mean value and associated uncertainty leads to a bolometric A_B of 0.24 ± 0.06 for Miranda and of 0.31 ± 0.06 for Ariel.

From ground-based photometry, the visual magnitudes $V(1,0)$ of Miranda and Ariel are 3.79 ± 0.17 and 1.48 ± 0.15, respectively (*18*). Combining these values with the newly determined radii of 242 ± 5 and 580 ± 5 km (*14*) yields geometric albedos (p_v) of 0.23 ± 0.04 and 0.33 ± 0.05. Where existing data sets overlap, the visible and near-infrared disk spectra of Ariel and Rhea are similar (*19*). From the Rhea data, we determined that the bolometric geometric albedo (p_B) of Rhea, normalized to its reflectivity at 0.56 μm, is 0.89. By assuming that this value is also representative of Miranda and Ariel, p_B (derived from p_v) is 0.20 ± 0.04 for Miranda and 0.30 ± 0.04 for Ariel; we have included an additional 5% uncertainty to allow for spectral differences between Rhea and the Uranian satellites. The phase integrals, equal to A_B/p_B, are therefore 1.17 ± 0.37 and 1.05 ± 0.25, respectively. These values are higher than expected for objects of relatively low albedo (*20*) and suggest a different surface microstructure, such as one composed of dark, relatively isotropically scattering grains (*17*).

REFERENCES AND NOTES

1. R. Hanel *et al.*, *Appl. Opt.* **19**, 1391 (1980).
2. R. Hanel, in *Spectrometric Techniques*, G. Vanasse, Ed. (Academic Press, New York, 1983), vol. 3, chap. 2.
3. G. Birnbaum and E. R. Cohen, *Can. J. Phys.* **54**, 593 (1976); E. R. Cohen and G. Birnbaum, *Natl. Bur. Stand. Intern. Rep. 80-2175* (1981); P. Dore, L. Nencini, G. Birnbaum, *J. Quant. Spectrosc. Rad. Transfer* **30**, 245 (1983); G. Bachet, E. R. Cohen, P. Dore, G. Birnbaum, *Can. J. Phys.* **61**, 591 (1983).
4. G. S. Orton, *Science* **231**, 836 (1986).
5. D. Gautier *et al.*, *J. Geophys. Res.* **86**, 8713 (1981).
6. B. Conrath, D. Gautier, R. Hanel, J. S. Hornstein, *Astrophys. J.* **282**, 807 (1984).
7. G. Lindal, personal communication; G. L. Tyler *et al.*, *Science* **233**, 79 (1986).
8. Y. Lebreton and A. Maeder, *Astron. Astrophys.*, in press; M. Casse, S. Cahen, C. Doom, *Proceedings of the Colloquium of the French Physical Society*, Nice, France, 9–13 September 1985.
9. A. Noels, R. Scuflaire, M. Gabriel, *Astron. Astrophys.* **130**, 389 (1984).
10. G. Orton *et al.*, *Icarus*, in press.
11. S. H. Moseley, B. J. Conrath, R. Silverberg, *Astrophys. J.* **292**, L83 (1985).
12. L. Wallace, *Icarus* **54**, 110 (1983); B. Bezard and D. Gautier, *Proceedings of the Conference on the Jovian Atmospheres*, New York, NY, 6–8 May 1985; J. Appleby, *Icarus*, in press.
13. J. R. Holton, *An Introduction to Dynamic Meteorology* (Academic Press, New York, 1979).
14. B. A. Smith *et al.*, *Science* **233**, 43 (1986).
15. J. Pirraglia, B. Conrath, M. Allison, P. Gierasch, *Nature (London)* **292**, 677 (1981).
16. J. Saari, R. Shorthill, D. Winter, *Moon* **5**, 179 (1972).
17. J. Goguen, personal communication; *Bull. Am. Astron. Soc.* **17**, 728 (1985).
18. D. P. Cruikshank, in *Uranus and the Outer Planets*, G. Hunt Ed. (Cambridge Univ. Press, Cambridge, England, 1982), p. 193.
19. R. N. Clark and P. D. Owensby, *Icarus* **46**, 354 (1981); R. H. Brown, *ibid.* **56**, 414 (1983).
20. R. Hanel *et al.*, *Science* **215**, 544 (1982).

21. We thank G. F. Lindal and G. L. Tyler of the radio science team for providing temperature profiles before publication; A. L. Lane for making computing facilities available to us; A. Ingersoll for many valuable comments; V. Suomi and R. Beebe for useful discussions; G. Orton for providing us with Fortran code for CH_4–H_2 absorption coefficients; and S. Akula, S. Bahethi, A. Gabbay, J. Guerber, L. Herath, P. Manava, L. Mayo, W. Shaffer, M. Silverstein, and J. Tingley for computer programming support.

31 March 1986; accepted 5 May 1986

Ultraviolet Spectrometer Observations of Uranus

A. L. BROADFOOT, F. HERBERT, J. B. HOLBERG, D. M. HUNTEN, S. KUMAR, B. R. SANDEL, D. E. SHEMANSKY, G. R. SMITH, R. V. YELLE, D. F. STROBEL, H. W. MOOS, T. M. DONAHUE, S. K. ATREYA, J. L. BERTAUX, J. E. BLAMONT, J. C. MCCONNELL, A. J. DESSLER, S. LINICK, R. SPRINGER

Data from solar and stellar occultations of Uranus indicate a temperature of about 750 kelvins in the upper levels of the atmosphere (composed mostly of atomic and molecular hydrogen) and define the distributions of methane and acetylene in the lower levels. The ultraviolet spectrum of the sunlit hemisphere is dominated by emissions from atomic and molecular hydrogen, which are known as electroglow emissions. The energy source for these emissions is unknown, but the spectrum implies excitation by low-energy electrons (modeled with a 3-electron-volt Maxwellian energy distribution). The major energy sink for the electrons is dissociation of molecular hydrogen, producing hydrogen atoms at a rate of 10^{29} per second. Approximately half the atoms have energies higher than the escape energy. The high temperature of the atmosphere, the small size of Uranus, and the number density of hydrogen atoms in the thermosphere imply an extensive thermal hydrogen corona that reduces the orbital lifetime of ring particles and biases the size distribution toward larger particles. This corona is augmented by the nonthermal hydrogen atoms associated with the electroglow. An aurora near the magnetic pole in the dark hemisphere arises from excitation of molecular hydrogen at the level where its vertical column abundance is about 10^{20} per square centimeter with input power comparable to that of the sunlit electroglow (approximately 2×10^{11} watts). An initial estimate of the acetylene volume mixing ratio, as judged from measurements of the far ultraviolet albedo, is about 2×10^{-7} at a vertical column abundance of molecular hydrogen of 10^{23} per square centimeter (pressure, approximately 0.3 millibar). Carbon emissions from the Uranian atmosphere were also detected.

THE VOYAGER ULTRAVIOLET SPECTROMETER (UVS), an objective-grating instrument, detects wavelengths from approximately 500 to 1700 Å by means of 126 contiguous channels and has a field of view 0°.1 by 0°.86.

Temperature and composition of the upper atmosphere. We measured the transmission of the Uranian atmosphere over 6000 km of altitude by recording light from the stars γ Pegasi and ν Geminorum and from the sun as each was occulted by Uranus' atmosphere (Table 1). When referred to a common geopotential (*1*), the occultations of the sun and γ Pegasi show similar transmission profiles at latitudes near 0° and near the light and dark poles, except for possible differences in the hydrocarbon profiles of up to one scale height.

Figure 1 shows light curves for three key wavelength regions (*2*). Continuum absorption by H_2 at wavelengths less than 845 Å (panel A) probes the highest levels; this range is accessible only in the solar occulta-